Advances in radiated power control at DIII-D

D. Eldon[*,a,b], E. Kolemen[b], D.A. Humphreys[a], A.W. Hyatt[a], A.E. Järvinen[c], A.W. Leonard[a], A.G. McLean[c], A.L. Moser[a], T.W. Petrie[a], M.L. Walker[a]

[a] General Atomics, PO Box 85608, San Diego, CA 92186-5608, United States
[b] Princeton University, Princeton, NJ 08544, United States
[c] Lawrence Livermore National Laboratory, PO Box 808, Livermore, CA 94550, United States

ARTICLE INFO

ABSTRACT

Feedback control of radiated power from the lower divertor $P_{rad, div, L}$ has been implemented in the DIII-D Plasma Control System (PCS). A realtime sensor for $P_{rad, div, L}$ has been constructed from 12 foil bolometer channels which agrees with standard post-shot analysis to within 20%. Results with the 12-channel sensor are compared to initial proof-of-concept tests with a single channel as a proxy for $P_{rad, div, L}$, showing that the upgraded sensor is necessary to overcome limitations of the proxy channel strategy in DIII-D. Using N_2 seeding under feedback control, $P_{rad, div, L}$ has been increased by up to 150% above unseeded levels, and a radiated power fraction f_{rad} of 80% has been demonstrated, although feedback controlled gas flow is steadier at $f_{rad} = 55\%$. Spatial coverage is broad enough to enable P_{rad} control during the strike point sweeps which are commonly used to generate pseudo-2D divertor Thomson measurements in DIII-D divertor experiments. Use of this control reveals challenges that may affect next step devices, which will require actively controlled extrinsic impurity seeding in order to manage heat loads. When operating at high f_{rad}, changes in pedestal T_e (caused by ELMs in these experiments but could come from other disturbances) resulted in large perturbations to P_{rad} which were destabilizing to the feedback controller.

1. Introduction and background

The DIII-D Plasma Control System (PCS) [1] has been upgraded to control radiated power from the divertor ($P_{rad, div, L}$) using N_2 seeding, up to a radiated power fraction f_{rad} of 80% and up to 150% increase above un-seeded levels. Future fusion devices like ITER or a reactor will have higher heat exhaust than present-day tokamaks (≈ 150 MW across the separatrix [2]), enough to damage the materials of plasma facing components unless properly mitigated by the edge and divertor plasma configuration. In order to keep peak heat flux below the ≈ 10 MW/m^2 steady state limit [3], about 70% of the power arriving in the scrape-off-layer (SOL) must be radiated [4–6]. Although high radiation fraction is necessary to protect plasma facing components, radiating too much power (such as by excessive impurity seeding/accumulation) can trigger a radiative collapse leading to disruption or interfere with H-mode operation: there is an optimal level of P_{rad}.

The control system discussed here is intended to maintain P_{rad} levels close to optimum by managing impurity seeding rates. This is useful for rapidly setting up experiments in present day devices and may be useful in ITER to protect the first wall. Impurity seeding is a standard method

for increasing P_{rad} [4,7,8] and will be required for ITER [8].

The advantages of developing P_{rad} control at DIII-D are that it can be exploited as a tool in DIII-D experiments, P_{rad} controlled plasmas can be studied with DIII-D's extensive diagnostic set (including examination of radiative divertor/mantle, impurity dynamics, impurity transport, and impact on pedestal performance), and a future attempt can be made to combine P_{rad} control with detachment control [9], as both are likely to be needed by ITER [10–12].

P_{rad} control has been studied at devices around the world, including the following examples:

ASDEX-U demonstrated P_{rad} control using estimates of P_{rad} from subsets of bolometer chords as the sensors and impurity puffing as the actuator [13,14]. ASDEX-U has also demonstrated control of power incident on the divertor, rather than power radiated by the plasma, by using shunt resistors in the tiles as the sensors [7].

Alcator C-Mod has demonstrated control of $P_{rad, div}$ using a single bolometer chord as a proxy measurement [15] and surface heat flux control using a set of surface thermocouples [16], both with N_2 puffing as the actuator.

Radiation control at EAST also uses bolometer fans and impurity

---

(mostly neon) seeding, but the availability of a supersonic molecular beam injection (SMBI) system allows much faster response times than gas puffing [17,18].

Past work on DIII-D [19] demonstrated a proof of concept controller for total P_{rad} with a set of 4 bolometer channels.

In this paper, DIII-D's P_{rad} control is upgraded with a system for constructing more accurate sensors and the ability to form sensors for radiation from specific zones of the plasma (e.g. core vs. divertor). This is a step towards eventually controlling the radiation *profile* by pairing zone-specific sensors with impurities which radiate in relevant T_e ranges. This paper describes control of P_{rad} from the divertor, first with a single proxy channel, then with an improved sensor constructed from 12 channels, which required upgrades to the connection between the PCS and bolometer digitizer. The setup of this system is described in Section 2, with results in Section 3, and then finally closing discussion in Section 4.

2. Radiation control system details

The radiation control system uses Proportional, Integral, Derivative (PID) feedback to obtain an actuator command (V_{com}) from the error between a measurement from a sensor and a requested value. All calculations are performed within the DIII-D PCS [1]. The actuators are piezoelectric gas inlet valves [20], and the sensor is constructed from foil bolometers [21]. Fig. 1 shows DIII-D's cross section marked with the positions of key actuators and diagnostics.

The power detected by each bolometer channel is given by Eq. 1 [21]:

$$P_{d,j} = \left(A_j \cdot \Delta V_{bol,j} + B_j \cdot \frac{d}{dt} \Delta V_{bol,j} \right) \tag{1}$$

where $\Delta V_{bol,\ j}$ are the measured voltage changes across a resistive thermometer since the beginning of the discharge (such that $\Delta V_{bol,\ j} \sim \Delta T_j$), and A_j and B_j are calibration constants. For each bolometer channel j, power detected $P_{d,\ j}$ can be converted into power radiated within the viewing volume $P_{rad,\ j}$ using Eq. 2 [21]:

$$P_{rad,j} = 2\pi R_j r_j \Delta \theta_j K_j P_{d,j} \tag{2}$$

where R_j is the major radius of the center of viewing chord j, r_j is the distance between the center of radiation from the detector, $\Delta \theta_j$ is the angular width of the viewing chord, and K_j is a constant of the detector and aperture geometry [21]. The location of the radiation source is estimated by reading the X-point location from realtime EFIT (RTEFIT) [22].

P_{rad} from a given region of the plasma can be found by performing a tomographic inversion or estimated by a linear combination of all the channels as in Eq. 3 for the lower divertor:

$$P_{rad,div,L} = \sum_j C_j P_{rad,j} \tag{3}$$

During standard post-shot analysis, all channels are available and can be used to form a fairly accurate estimate in lieu of performing tomography. In real time, only 12 channels are available, forcing $C_j = 0$ for most of the system. This requires some simplifying assumptions to build an estimate for the reduced set; namely that the dominant radiation source is in the lower divertor and that the channels pick up negligible contributions as they pass through other parts of the plasma. With more channels available post-shot, it is possible to construct a linear combination with compensation for radiation pickup from other parts of the plasma. Conveniently, the DIII-D bolometer system has been designed so that total radiation is given by the sum over all channels in a fan [21]; thus $C_j = \frac{1}{2}$ for all of the real-time channels in use, which are split between two fans (see Fig. 1). A new toolbox was added to the OMFIT framework for scientific tasks [23] to test different combinations of channels and find the best subset of channels to use for this purpose, prior to upgrading the PCS–bolometer interface to increase the number

of real-time channels from 4 to 12.

The particular combination of chords from two fans essentially amounts to estimating $P_{rad,\ div,\ L}$ twice and taking the average. The estimates from each fan, their average, and the standard post-shot result are plotted in Fig. 2, showing that the real time estimate for $P_{rad,\ div,\ L}$ agrees with the standard post-shot estimate to within 20%. The estimate for $P_{rad,\ div,\ L}$ remains valid even when the shape changes such as during a strike point sweep. Example plasma boundaries at the end-points of such a sweep are shown in Fig. 1.

It's also worth noting that some scenarios entail significant radiation from the lower floor, where the lower divertor shelf obstructs the view of the lower bolometer fan and would cause an underestimation of P_{rad} from that fan. The inner strike point passed through the obscured region during the strike point sweeps tested during control development, which probably explains why the realtime estimate for $P_{rad,\ div,\ L}$ is below the post-shot estimate until about 4000 ms, when the inner strike point moves onto the shelf (see Fig. 2).

Fig. 3 shows how the proxy and upgraded real-time estimates for $P_{rad,\ div,\ L}$ track the standard post-shot estimate in cases of swept and fixed strike points: a proxy channel may be enough for some fixed-shape cases, but the upgraded sensor is needed if the plasma boundary moves significantly.

These experiments were carried out in lower single null plasmas with the outer strike point on the lower divertor shelf (see Fig. 1) in most cases. Key plasma parameters are given in Table 1.

Tuning is done by calculating initial PID settings based on system identification and then refining gains after seeing results. System identification is performed by stepping V_{com} and fitting the response in P_{rad} to a First Order Plus Dead Time (FOPDT [24]) model to obtain the static gain K_s, dead time or lag L, and e-folding timescale $\mathcal{T}$. A reasonable starting point seems to be a modified Ziegler-Nichols [25] tuning with proportional gain reduced by 50% and integral and derivative timescales the same: $G_p = 1.2\mathcal{T}/(K_s L) \times 0.5$, $\tau_I = 2L$, $\tau_D = L/2$. The FOPDT analysis and initial PID tuning calculation can easily be performed between shots using a dedicated utility [9] which has now been ported into OMFIT [23].

The gas species being puffed should be one which radiates more than deuterium within some relevant temperature range. Nitrogen is a good radiator at typical DIII-D divertor temperatures ($\sim$ 1–50 eV). Nitrogen data fit well to the FOPDT model and have about 2.5 times stronger response to N_2 seeding in divertor radiation than in core radiation. N_2 has also been used to control total or divertor radiation in devices including ASDEX [14] and C-MOD [15,16], with other gasses (Ne [13,17,19], Ar [14]) used to control core radiation. EAST must avoid N_2 and thus has developed divertor radiation control using Ne [17].

3. Results of radiation control experiments

Preliminary tests of P_{rad} control were carried out using an individual

Table 1
Plasma parameters for radiation control tests and applications with the proxy chord strategy and the upgraded sensor using multiple bolometer chords.

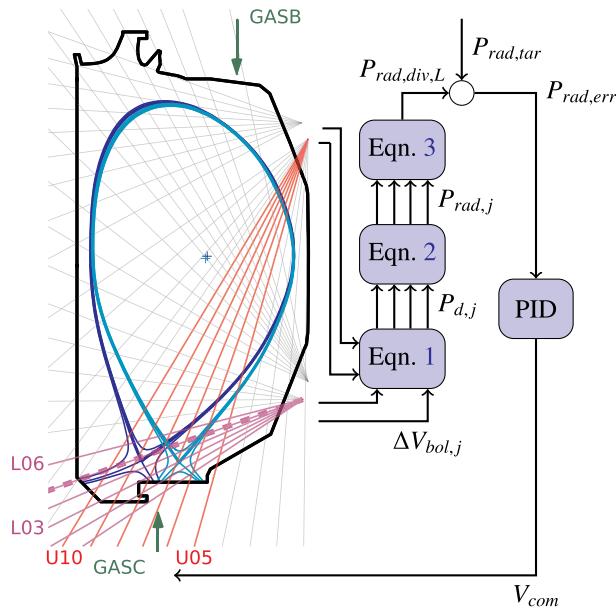| Sym.	Proxy	Multi-ch	Units	Description
I_p	1.3	0.6, 0.9, 2.0	MA	Plasma curr.
B_T	-2.1	$\pm$ (1.8–2.2)	T	Toroidal field
β_N	1.7–2.2	1.6–2.9		Norm. beta
q_{95}	3.6	3.6, 4.8, 11		Safety factor
P_{INJ}	5.5	3.4–14	MW	Beam power
R	1.7	1.7–1.9	m	Major radius
a	0.6	0.6	m	Minor radius
κ	1.7	1.8–1.9		Elongation
$\langle n_e \rangle$	7–10	3.3–9.0	$10^{19} \mathrm{m}^{-3}$	Avg. density
$p_{e,\ ped}$	3.2	1–10	kPa	Ped. e$^-$ press.
$T_{e,\ ped}$	340	250–950	eV	Ped. e$^-$ temp.

Fig. 1. DIII-D cross section and control schematic. Cross section overlays: limiting surfaces (black), sample plasma last closed flux surfaces (blue and cyan at 2000 and 5000 ms), bolometer proxy channel (thick dashed magenta), bolometer channels used by upgraded sensor (red and magenta), unused bolometer channels (faint gray), and gas injection ports (green arrows). (For interpretation of the references to colour in this figure legend, the reader is referred to the web version of this article.)
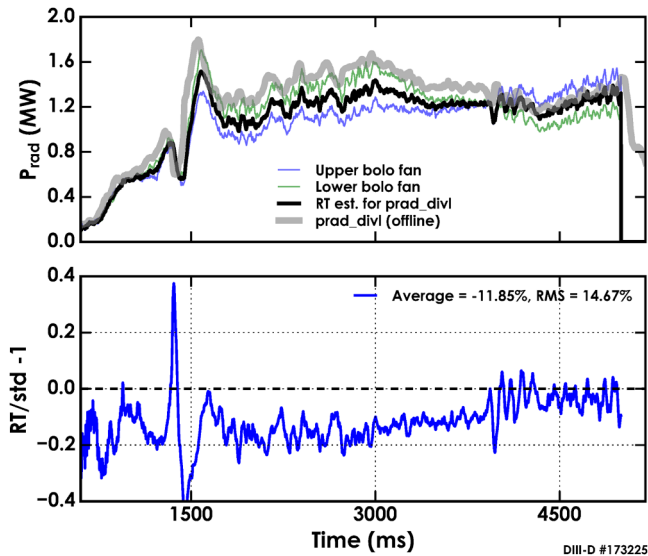

Fig. 2. Construction of the RT estimate for $P_{rad, div, L}$ by averaging two fans and comparison to standard post-shot analysis. Top: results from standard post-shot analysis (gray), result from RT analysis in the PCS (black), and contributions from the two fans, which are averaged to produce the RT result (blue and green). Bottom: Comparison between the RT and standard post-shot estimates for $P_{rad, div, L}$, showing that the RMS difference is < 20%. (For interpretation of the references to colour in this figure legend, the reader is referred to the web version of this article.)

bolometer channel selected to serve as a proxy for the divertor radiating zone and impurity seeding through a gas inlet port in the divertor (see Fig. 1). N_2 puffing into the divertor was used to control divertor radiation with results shown in Fig. 4. In addition to extrinsic N_2 seeding, DIII-D plasmas always have an appreciable carbon content from the graphite walls, which is typically the dominant source of intrinsic radiation.

Fig. 4(b) shows proxy P_{rad} from a shot with control and one without any N_2 puffing as well as the target value. P_{rad} increases in response to puffing with a delay consistent with system identification, then decreases after control is deactivated, again with a delay consistent with expectations. However, we must consider whether the proxy measurement, which we can control, adequately represents the true $P_{rad, div, L}$, which is more accurately estimated by post-shot techniques which have access to all of the bolometer channels [21]. Fig. 4(d) is a counterpart to 4(b), showing $P_{rad, div, L}$ from standard post-shot analysis with an estimated equivalent target for comparison. The estimated target is the proxy's target times the ratio of the average standard analysis result times the average proxy measurement. As seen in the figure, the standard analysis result doesn't appear to track the equivalent target as well as the proxy measurement tracks the literal target. This is because increasing P_{rad} causes the radiation source to move farther upstream and out of view of the proxy channel. A more severe manifestation of this problem occurs when the average T_e in the volume imaged by the proxy channel falls below the peak in nitrogen's radiative loss parameter $L_Z(T_e)$ (see Fig. 1 of Kallenbach, et al. [26]), at which point additional N_2 seeding causes local P_{rad} to decrease further as more energy is radiated upstream. Since the slope between P_{rad} and puffing has switched sign, the controller will peg V_{com} to its limit and never recover.

This problem was solved by constructing a higher quality sensor from 12 bolometer chords, which became possible after the connection between the PCS and bolometer system was upgraded to acquire more channels. With the upgraded sensor, the radiation peak tends to stay within view of the bolometer set and the problem with detected P_{rad} decreasing with additional puffing has not been observed. The upgraded system was used successfully in divertor experiments using shape changes to sweep the strike point past key diagnostics, which is a common technique in DIII-D [27]. The range of a typical sweep is within the view of the bolometer fans shown in Fig. 1.

Figs. 5, 6, and 7 show P_{rad} control performance with the upgraded sensor in divertor experiments with strike point sweeps. In each figure, the top panel compares P_{rad} during feedback control of N_2 seeding, the target P_{rad} level, and P_{rad} from the last shot before N_2 seeding (referred to as baseline P_{rad}). The middle panel shows ratios between P_{rad} with N_2 and baseline P_{rad}, between the target and baseline, and between controlled P_{rad} and the target. This quantifies how much P_{rad} increased and how well P_{rad} conforms to the target value. f_{rad} in these shots ranged from 30–80% and RMS deviation from target was $\leq 20\%$, with details given in Table 2. The reduction in inter-ELM peak heat flux near the outer strike point as measured by including infrared television (IRTV) [28] was about 30% between shots 173236 and 173224 (100% higher P_{rad}), but was insignificant between 173225 and 173224 (30% more radiation). Based on the heat flux profiles in Fig. 8, it seems that conducted heat flux *is* being reduced substantially, but that these reductions are partially replaced by increased radiated heat flux to the target. This is consistent with both bolometer data and the design of the controller, which aims to increase local divertor radiation. Clearly, more P_{rad} will be needed farther from the divertor, but this poses its own challenges, as impurities like Ne and Ar, which radiate at higher T_e, tend to degrade core performance [15] and increase risk of radiative collapse. IRTV was not available for shot 172510 (Fig. 7).

The case shown in Fig. 6 develops a large, periodic oscillation in P_{rad}. This appears to be caused by both limitations of the control system and by the behavior of the plasma at high f_{rad}. During the phases of low P_{rad}, the plasma is ELM-free and the pedestal height increases. When a large ELM reduces pedestal temperature, P_{rad} increases and maintains a low pedestal height (in both T_e and n_e) until ELMs stop again. Smoothing is required prior to Eq. 1 due to the $d\Delta V/dt$ term, which introduces a lag to P_{rad} in the PCS. This lag is not usually a serious problem, as evidenced by better performance in Figs. 5 and 7. However, at high f_{rad}, cooling of the pedestal by ELMs causes large changes in P_{rad} on the ~ 10 ms timescale, which is shorter than the smoothing time constant. The realtime and standard post-shot estimates for P_{rad}, which
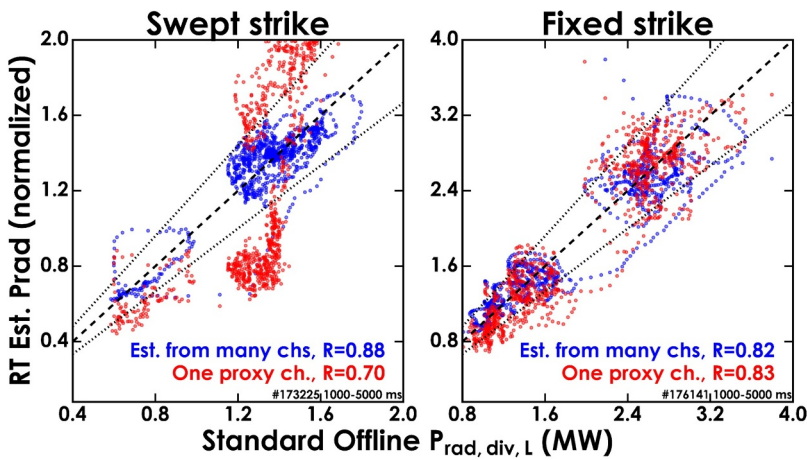
Fig. 3. Correlations between realtime estimators and standard post-shot analysis for shots with swept (left) and fixed (right) strike points. Right: Either method would work for fixed strike point, given the correct choice of proxy. Left: Changing plasma boundary shape during a shot, as in a strike point sweep, breaks the single-proxy-channel strategy as the optimal channel to pick changes with shape. However, the multi-channel estimate is robust to this shape change.
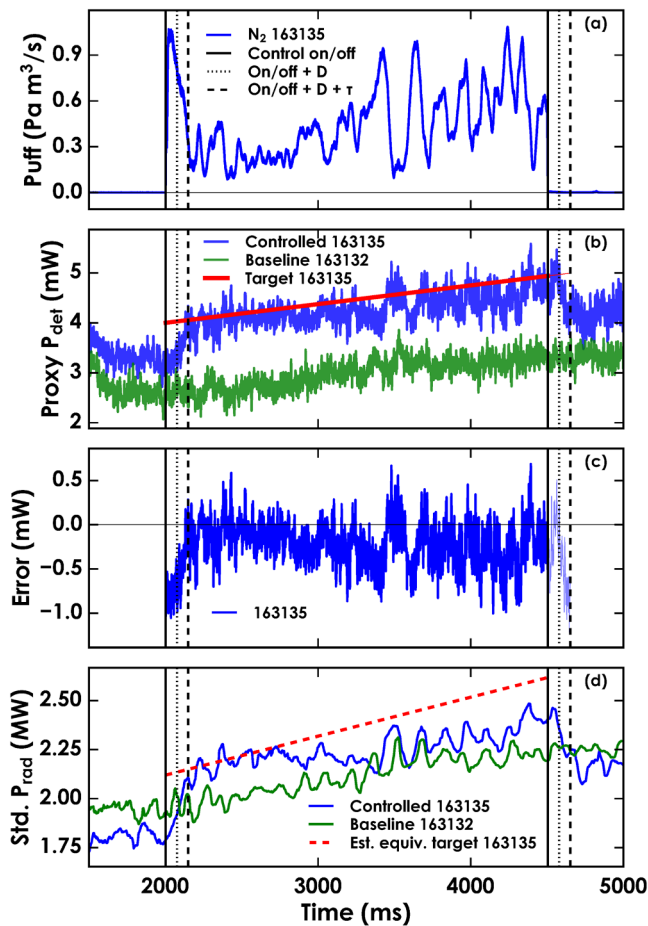

Fig. 4. Control of $P_{rad,\ div,\ L}$ by local N_2 seeding (GASC port; see Fig 1). (a) N_2 gas flow rate vs. time; solid vertical lines mark when control is on, dotted and dashed vertical lines are delayed relative to control on/off by L and $\mathcal{T}$. (b) Local P_{rad} measurement from a single bolometer chord used as a proxy for $P_{rad,\ div,\ L}$ from the controlled (blue) and reference (green) shots. The target used during control is shown as a solid red line. (c) Error between the local proxy measurement and its target (blue - red from panel (b)). (d) $P_{rad,\ div,\ L}$ obtained by standard automatic analysis of all relevant bolometer channels. The dashed red line is the estimated effective target, obtained by multiplying the target from (b) by the average ratio between the proxy measurement and the standard $P_{rad,\ div,\ L}$. (For interpretation of the references to colour in this figure legend, the reader is referred to the web version of this article.)
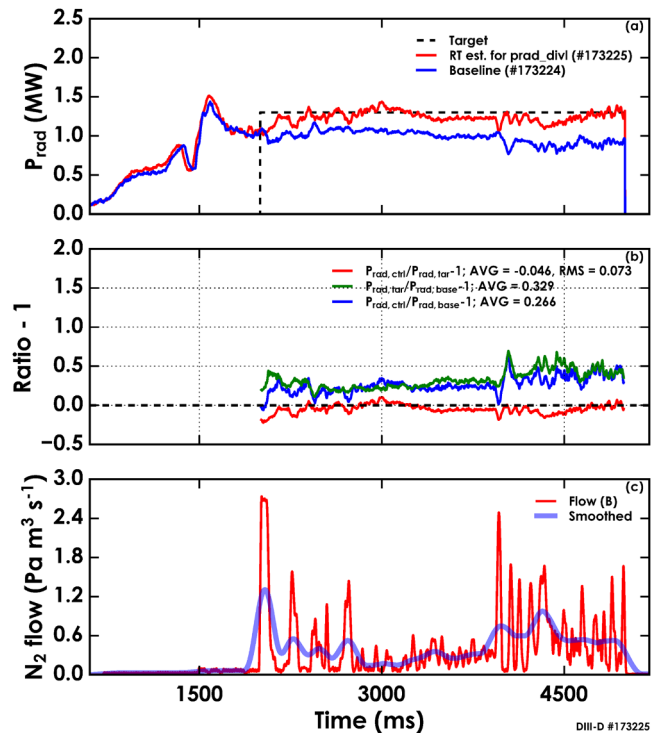

Fig. 5. Control of $P_{rad,\ div,\ L}$ by N_2 seeding with increase of 30% relative to unseeded. (a) $P_{rad,\ div,\ L}$ as estimated by PCS for a baseline shot without impurity seeding (blue), for a shot with N_2 seeding under feedback control (red), and the target for the controller. (b) Ratios between $P_{rad,\ div,\ L}$ measurements and target showing that the feedback target was 33% higher than the baseline radiation level and the RMS difference between controlled $P_{rad,\ div,\ L}$ and the target was < 10%. (c) Feedback controlled N_2 gas flow through port GASB (see Fig 1). (For interpretation of the references to colour in this figure legend, the reader is referred to the web version of this article.)

use causal and acausal smoothing filters, are out of phase with each other when measuring the oscillation in P_{rad} seen in Fig. 6. Despite this, it can be seen that lag in the realtime P_{rad} sensor is only exacerbating an existing problem, not causing it completely: Fig. 9 shows results from the next shot, where feedback control was replaced by averaging V_{com} associated with the large oscillation and programming it in feedforward. It can be seen that although the P_{rad} oscillation is smaller, it is still present.
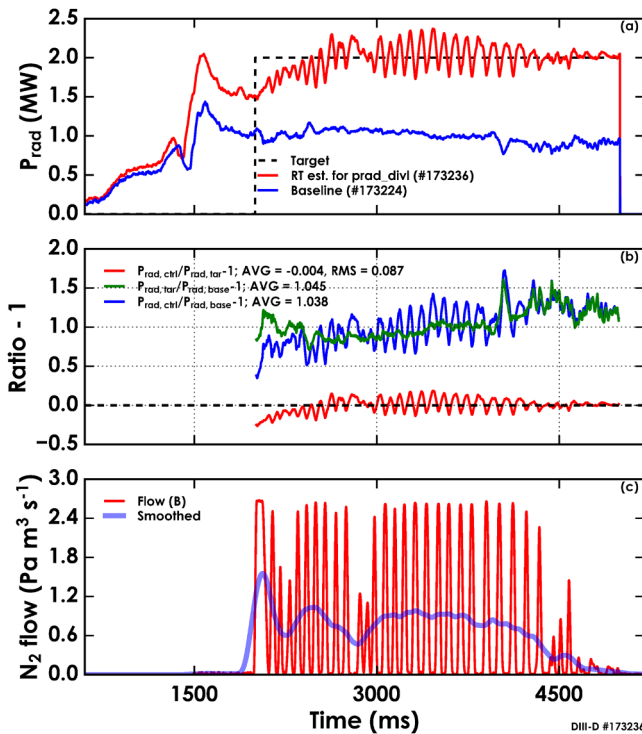
Fig. 6. Control of $P_{rad, div, L}$ by N_2 seeding with increase of 100% relative to unseeded. Compare to Fig. 5, which has the same setup except for P_{rad} target. As this is several shots later, the walls have been loaded with N_2, providing an additional source relative to Fig. 5. An oscillation in P_{rad} has developed and the controller is responding by switching N_2 flow on and off quickly.
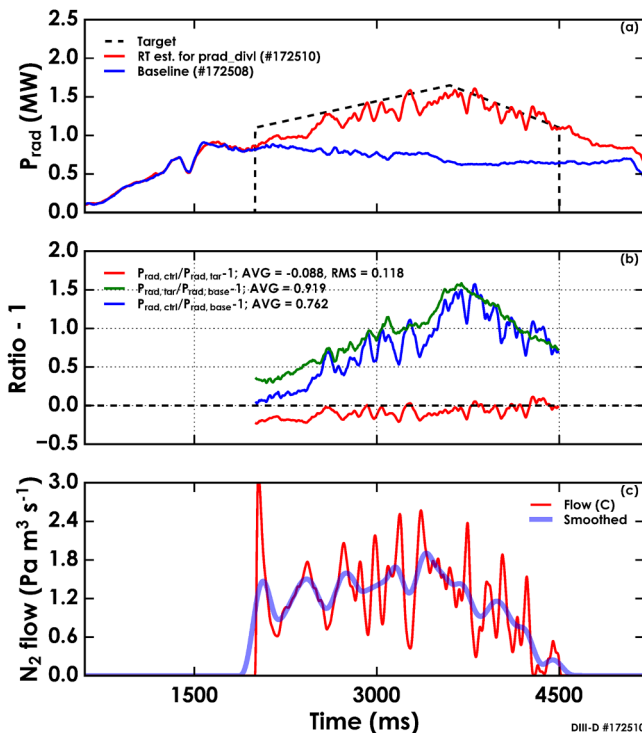

Fig. 7. Control of $P_{rad, div, L}$ by local impurity seeding through injector GASC (see Fig. 1) into the private flux region with increase of 80% on average (peaking briefly at 150%) relative to unseeded case. Compare to Figs. 5 and 6, which fueled from injector GASB in the main chamber.

Table 2
P_{rad} control results from representative shots with control.

ΔP_{rad}	RMS vs. target	f_{rad}	Shot (Fig)
30%	7%	30%	173225 (5)
40%	18%	70%	177022
60%	13%	50%	173192
65%	20%	60%	176141
100%	9%	80%	173236 (6)
0–150–80%	12%	35–55–40%	172510 (7)
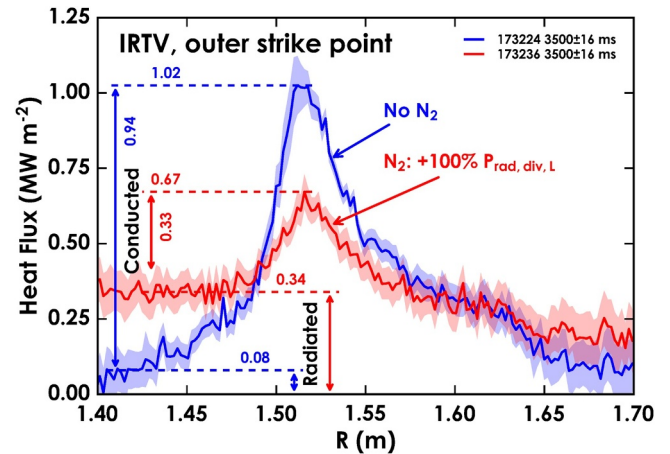
Fig. 8. Comparison of IRTV heat flux profiles at the outer divertor target for cases with (red) and without (blue) heavy N_2 seeding. Despite increasing $P_{rad, div, L}$ by 100% (see Fig. 6), the N_2 seeding case does not experience dramatic decrease in peak heat flux. It appears that reductions in conducted heat flux have been partially replaced by increases in radiated heat flux. (For interpretation of the references to colour in this figure legend, the reader is referred to the web version of this article.)
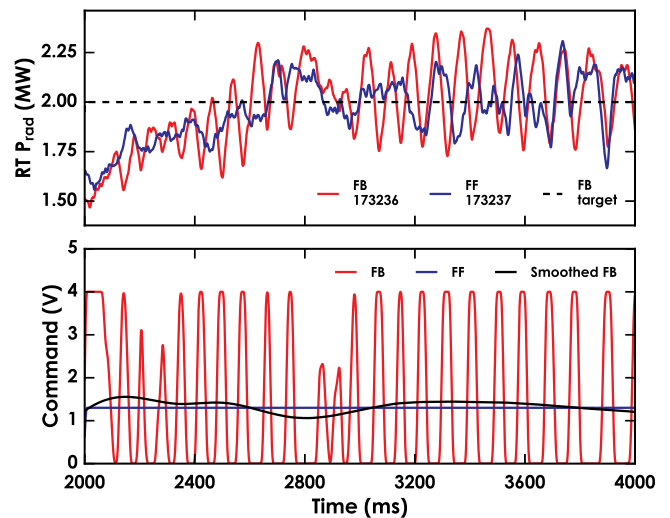

Fig. 9. In the case shown in Fig. 6, P_{rad} was at the target on average, despite large oscillations. The time average of V_{com} from that case was used as constant feedforward V_{com} in the next shot. As shown by the blue trace in the top panel, there is still some fluctuation in P_{rad}, even with constant V_{com}. (For interpretation of the references to colour in this figure legend, the reader is referred to the web version of this article.)

4. Discussion and conclusion

Feedback control of divertor radiated power $P_{rad, div, L}$ using N_2 seeding has been demonstrated at DIII-D with the ability to increase $P_{rad, div, L}$ by > 100% above un-seeded levels up to a total radiation

fraction of $\approx 80\%$. A high quality sensor constructed from several bolometer channels viewing the divertor is needed to keep the radiation source in view as it moves due to changes in plasma conditions during impurity seeding (this may be specific to DIII-D's bolometer or divertor geometry: a good estimate for $P_{rad, \, div, \, L}$ has been obtained from a single bolometer channel in ASDEX-U [14]). This control has begun to see regular use at DIII-D and the system will next be expanded to acquire all 48 bolometer channels in real time. Access to more channels will enable higher quality estimates using more sophisticated linear combinations of channels. The PCS will be upgraded to provide consistently available real-time estimates for radiation from upper and lower divertors, the core plasma, and the total.

As some form of P_{rad} control will be required for material protection in ITER, it is important to gain experience using P_{rad} control now so that we can discover unexpected benefits, limitations, and interactions with other feedback control systems. Development of P_{rad} control at DIII-D compliments experience being gained by related systems on other tokamaks with different parameter ranges, while also providing a useful tool locally.

Acknowledgements

References

[1] J.R. Ferron, et al., (Proc. 16th IEEE/NPSS Symp. on Fusion Engin.), (1995), https://doi.org/10.1109/FUSION.1995.534361.

[2] F. Ryter, et al., Nucl. Fusion 36 (1996) 1217, https://doi.org/10.1088/0029-5515/36/9/11.

[3] A. Loarte, et al., Nucl. Fusion 47 (2007) S203, https://doi.org/10.1088/0029-5515/47/6/S04.

[4] R.A. Pitts, et al., Phys. Scr. T138 (2009) 014001, https://doi.org/10.1088/0031-8949/2009/T138/014001.

[5] A. Loarte, et al., Proceedings of the 22nd IAEA Fusion Energy Conference in Geneveva, (2008).

[6] A.S. Kukushkin, et al., Nucl. Fusion 49 (2009) 075008, https://doi.org/10.1088/0029-5515/49/7/075008.

[7] A. Kallenbach, et al., Plasma Phys. Control. Fusion 52 (2010) 055002, https://doi.org/10.1088/0741-3335/52/5/055002.

[8] C. Guillemaut, et al., Plasma Phys. Control. Fusion 59 (2017) 045001, https://doi.org/10.1088/1361-6587/aa5951.

[9] D. Eldon, et al., Nucl. Fusion 57 (2017) 066039, https://doi.org/10.1088/1741-4326/aa6b16.

[10] A.W. Leonard, et al., Nucl. Fusion 52 (2012) 063015, https://doi.org/10.1088/0029-5515/52/6/063015.

[11] A. Loarte, et al., Nucl. Fusion 38 (1998) 331, https://doi.org/10.1088/0029-5515/38/3/303.

[12] E. Kolemen, et al., J. Nucl. Mater. 463 (2015) 1186, https://doi.org/10.1016/j.jnucmat.2014.11.099.

[13] A. Kallenbach, et al., Nucl. Fusion 35 (1995) 1231, https://doi.org/10.1088/0029-5515/35/10/I07.

[14] A. Kallenbach, et al., Nucl. Fusion 52 (2012) 122003, https://doi.org/10.1088/0029-5515/52/12/122003.

[15] J.A. Goetz, et al., Phys. Plasmas 6 (1999) 1899, https://doi.org/10.1063/1.873447.

[16] D. Brunner, et al., Nucl. Fusion 57 (2017) 086030, https://doi.org/10.1088/1741-4326/aa7923.

[17] K. Wu, et al., Nucl. Fusion 58 (2018) 056019, https://doi.org/10.1088/1741-4326/aab506.

[18] B.J. Xiao, et al., Fusion Eng. Des. 128 (2018) 90, https://doi.org/10.1016/j.fusengdes.2018.01.045.

[19] G.L. Jackson, et al., J. Nucl. Mater. 241 (1997) 618, https://doi.org/10.1016/S0022-3115(97)80110-9.

[20] S.C. Bates, et al., Rev. Sci. Instrum. 55 (1984) 934, https://doi.org/10.1063/1.1137845.

[21] A.W. Leonard, et al., Rev. Sci. Instrum. 66 (1995) 1201, https://doi.org/10.1063/1.1146006.

[22] J.R. Ferron, et al., Nucl. Fusion 38 (1998) 1055, https://doi.org/10.1088/0029-5515/38/7/308.

[23] O. Meneghini, et al., Nucl. Fusion 55 (2015) 083008, https://doi.org/10.1088/0029-5515/55/8/083008.

[24] E. Kolemen, et al., Nucl. Fusion 50 (2010) 105010, https://doi.org/10.1088/0029-5515/50/10/105010.

[25] J.G. Ziegler, et al., Transactions of the ASME 64 (1942) 759.

[26] A. Kallenbach, et al., Plasma Phys. Control. Fusion 55 (2013) 124041, https://doi.org/10.1088/0741-3335/55/12/124041.

[27] A.G. McLean, et al., J. Nucl. Mater. 463 (2015) 533, https://doi.org/10.1016/j.jnucmat.2015.01.066.

[28] C.J. Lasnier, et al., Nucl. Fusion 38 (1998) 1225, https://doi.org/10.1088/0029-5515/38/8/209.